

# Experimental assessment and simulation of surface nanocrystallization by severe shot peening

S.M. Hassani-Gangaraj <sup>a,b,\*</sup>, K.S. Cho <sup>a,c</sup>, H.-J.L. Voigt <sup>a</sup>, M. Guagliano <sup>b</sup>, C.A. Schuh <sup>a</sup>

<sup>a</sup> Department of Materials Science and Engineering, Massachusetts Institute of Technology, Cambridge, MA 02139, USA

<sup>b</sup> Department of Mechanical Engineering, Politecnico di Milano, Milan 20156, Italy

<sup>c</sup> Center for Advanced Materials Technology (CAMT), Kookmin University, Seoul 136-702, Republic of Korea

Received 11 March 2015

Revised 22 June 2015

Accepted 24 June 2015

## 1. Introduction

Most material failures, including fatigue fracture, fretting fatigue, wear and corrosion are very sensitive to the structure and properties of a material's surface, and many of these properties are known to improve in fine grained and nanocrystalline (NC) materials [1,2]. As a result, methods to achieve a nanocrystalline surface layer over bulk material are of broad interest, especially since surface nanocrystallization [3] processing techniques may bypass difficulties of synthesizing bulk NC components and yet exploit the advantages of NC materials in service. Mechanically induced surface nanocrystallization is generally effected through repeated multidirectional plastic deformation caused by high velocity impacts. Such impacts create high dislocation densities through strain localization in shear bands, followed by recombination, rearrangement and annihilation of some dislocations upon subsequent impact events. The initial grains are thereby subdivided into a large number of sub-grains (or domains) separated by small angle grain boundaries [3,4], which can also gradually accumulate misorientation to become high-angle boundaries. Equiaxed ultrafine or nano grains with random crystallographic

orientation have been found by TEM observation in a variety of studies of this kind [4–6].

A variety of shot peening derived processes have been developed, although they all fundamentally exploit the same materials mechanics and structural evolution mechanisms to achieve surface nanocrystallization. For example, ultrasonic shot peening (USSP), sometimes called surface mechanical attrition (SMAT) [4–13] uses a dynamic generator at frequencies ranging from 50 Hz to 20 kHz, to resonate peening media against a sample surface. Air blast shot peening employs compressed air to accelerate shots, and is widely used industrially because of its simplicity, low cost and applicability to variety of targets. Air blast shot peening becomes a severe process that accesses ultrafine and NC structures when certain combinations of peening parameters are used to multiply the kinetic energy of the shot impacts [14–18]. In general, we differentiate severe shot peening [19–21] from conventional shot peening in order to emphasize its aim at generating ultra-fine grained or NC surface layers.

Surface nanocrystallization mechanisms can be related to the magnitude of the stacking fault energy [22]. In materials with larger stacking fault energy such as iron, TEM observations after SMAT revealed that dense dislocation walls and tangles are generated inside the original grains. Upon further straining, the dislocation walls and tangles transform into sub-boundaries with small misorientation via annihilation and rearrangement in order to minimize the total energy of the system. Eventually, sub-grain

\* Corresponding author at: Department of Materials Science and Engineering, Massachusetts Institute of Technology, Cambridge, MA 02139, USA.

E-mail address: mhassani@mit.edu (S.M. Hassani-Gangaraj).

boundaries evolve into high-angle grain boundaries that subdivide the original grains into refined structures [23]. In low stacking fault energy materials such as austenitic stainless steel, the prominent features include planar dislocation arrays and mechanical micro-twins at higher strains [6,10]. The original coarse grains thus become sub-divided by lamellar twins with nanometer-sized thickness. Upon further straining dislocations inside the lamella arrange themselves into dislocation walls traversing the thickness of the microtwin lamellae. Twin-twin intersection also leads to nanometer sized blocks. In the case of SMATed copper (medium stacking fault energy) intermediate behavior with two different mechanisms of refinement is observed [12]. In the subsurface layer, dislocation activity leads to dislocation cells instead of tangles, but at the top surface layer (within 25  $\mu\text{m}$ ), the twinning-related refinement mechanisms seen in low stacking fault energy materials are operative.

Modeling of nanocrystallization mechanisms during severe shot peening has not been extensively treated. In Ref. [24] a finite element analysis of the mechanics of peening was presented. However, no connection was given to the microstructural evolution process, grain size and the gradient of nanostructure that naturally evolves during peening. A physical model of structure evolution would be useful to engineer the surface layers and design a peening process to attain a desired nanostructure.

It is the purpose of this paper to present a systematic study of surface nanocrystallization by severe shot peening. Using air blast peening, a wide range of coverage was adopted to span both conventional and severe shot peening regimes. A hybrid numerical model was developed with the aim of assessing microstructural evolution during shot peening. Scanning electron microscopy (SEM) and transmission electron microscopy (TEM) observations were conducted to study the grain refinement, surface nanocrystallization and also for comparison with a finite element simulation incorporating dislocation density evolution. The comparison of dislocation cell size obtained by numerical framework and those measured by TEM/SEM observation shows a satisfactory and promising agreement.

## 2. Material and experiments

The substrate material considered in this study is high strength low alloy steel ESKYLOS6959 (equivalent to DIN 35NiCrMoV12-5 or AISI 4340). Its chemical composition is summarized in Table 1. AISI 4340 is one of the most widely studied materials after shot peening. The reason is that its application is mainly power transmission gears, shafts and aircraft landing gears where fatigue is always the first design consideration, and shot peening has been widely applied to these components to improve fatigue behavior.

Cylindrical specimens of 7.52 mm diameter in the target section were machined from a forged bar. All specimens were extracted from the bar in the same radial position to ensure similarity of microstructure. The bar had been quenched from 880  $^{\circ}\text{C}$  in water and then tempered at 635  $^{\circ}\text{C}$  for 5 h.

Standard cast steel shots, S230, were accelerated in an air blast machine to conduct shot peening. Shot peening was performed with 100%, 200%, 650%, 1000% and 1300% coverage to examine the evolution of microstructure as coverage increases. 100% and sometimes 200% are the typical coverage levels used in conventional shot peening to generate an appropriate field of compressive

residual stress and sufficient work hardening. The higher levels of 650%, 1000% and 1300% represent the severe shot peening regime, in which significant grain refinement and eventually surface nanocrystallization are produced. Shot peening coverage can be effectively related to the peening time. For instance, for a given target area and set of peening parameters, the time needed to attain a coverage of 1000% is ten times the time needed to attain the full coverage (100%). The angle between the shot flow and the target surface in the experiment was set equal to 90 $^{\circ}$  for simplicity, and because this is a recommended angle for uniform residual stress generation. Randomly deviating from perpendicular impacts might also be beneficial in terms of inducing very localized multidirectional severe plastic deformation. The shot peening intensity as measured on "Almen A" strip was 18, which is an index of the total energy of the treatment. Using the approach of Ref. [25], we may connect the Almen intensity to the shot flow velocity for a fixed shot; in this manner the effect of shot velocity on nanocrystallization can be inferred for practical applications.

The microstructure of peened samples was characterized using a JEOL 2010F analytical microscope operated at 200 kV and FEI/Philips XL30 FEG ESEM at 20 kV. The peened samples were mechanically cross sectioned, polished and mounted on copper grids for TEM observation. To prepare TEM specimens, two cylindrical disks were prepared first by cutting the shot-peened specimens. These disks were glued face-to-face on a metal plate, and then mechanically polished to make thin foils. This procedure was needed to preserve a disk edge that included the severely deformed layer (top surface), as well as observe the non-deformed layers simultaneously. The two polished parts of the disk were then re-glued onto a slot grid, and were ion-milled using a Gatan PIPS instrument with an ion accelerating voltage of 5 kV at 5 $^{\circ}$ . The distance of a given observed region from the free surface was measured in the TEM using low-magnification imaging. The mean grain size was evaluated from layers within a vertical range of 5  $\mu\text{m}$ . SEM observations were also conducted to evaluate grain refinement. 8% Nital was used as etchant to reveal the final microstructure (i.e., lower bainite and/or tempered martensite) with the cell boundaries. All the SEM observations were conducted under the same magnification factor of 2000X to attain better statistics. The cell (and/or grain) sizes reported are area-equivalent circular diameter for structures that are dominated by equiaxed cells, and length for the structures dominated by lamellar cells [26]. The total counts for each size measurement was at least above 70. For the low coverage levels (100% and 200%), it was difficult to use TEM because of the relatively coarse grains and the correspondingly limited view of the relevant structural scales, which are coarser than the TEM observations. Similarly, for high coverage levels (650%, 1000% and 1300%), the refined grains were too small to evaluate by SEM.

## 3. Numerical framework

### 3.1. Finite element simulation

Finite element models of a single impact and multiple impacts are developed and linked to a dislocation density evolution model. The single impact model, as the unit process of peening, was used to examine the effect of media size, velocity and hardness on the induced refinement. Multiple impacts model was used to realistically simulate the induced refinement by peening with different coverage levels, from 100% to 1300%.

Two dimensional axisymmetric models of a target impinged upon by a single impact were developed with the commercial finite element code Abaqus Explicit 6.10-1 [27]. The dimension of the target was chosen to be  $5R \times 5R$ , where  $R$  is the shot radius,

**Table 1**  
Chemical composition of the present high strength low alloy steel (wt%).

C	Mn	Si	Cr	Mo	Ni	V	Fe
0.3–0.4	0.4–0.9	0.15–0.55	1–2	0.35–0.9	2.5–4.5	0.05–0.25	Balance

to ensure boundary conditions do not interfere with the elasto-plastic deformation occurring in the surface layer. Only the lower half of the shot was modeled to reduce the computation time. However, its density was doubled to convey the same kinetic energy as the full shot. CAX4R [27], which is a 4-node bilinear axisymmetric quadrilateral element with reduced integration and hourglass control, was used to discretize both target and shot. Interface contact elements were introduced using the penalty algorithm [27] with a Coulomb friction coefficient of 0.2. The target's bottom was constrained against all degrees of freedom, and the initial shot velocity was set to a value in the range of 20–200 m/s (with 65 m/s matching the experimental value), applied to all of the shot's nodes. This is the velocity range adopted for practical peening. Higher impact velocities would cause an intolerable surface roughness or even abrasion, while at lower impact velocities plastic deformation of materials of technical interest is not likely. In order to study the effect of media size on the refinement, a range of 0.2–1.2 mm diameter balls were simulated, with 0.6 mm matching the size of the shot used in the experiments. Appropriate damping parameters [28] were introduced into the model in order to prevent residual oscillations. Fig. 1a shows the finite element model of a single impact and the corresponding boundary conditions.

An elastic-perfectly plastic behavior was applied to simulate the shot behavior, with a yield stress ( $Y$ ) in the range of 1550–2500 MPa (with 1550 MPa matching the experimental value based on the expectation that steel shot has a hardness range of 40–52 Rockwell C). The density  $\rho = 7850 \text{ kg/m}^3$ , Young's modulus  $E = 210 \text{ GPa}$  and Poisson's ratio  $\nu = 0.3$  were also used.

Strain rate plays a major role in dictating the level and distribution of the residual stress field, and the induced plastic strains due to shot peening [28]. Therefore, it is crucial that the target's constitutive behavior is able to reflect not only an appropriate hardening law as a function of plastic strain but also the strain rate sensitivity of the flow stress. The Johnson–Cook constitutive equation [29] originally tested and proposed for metallic materials such as 4340 steel was applied for the target. It expresses the flow stress as a function of equivalent plastic strain, strain rate and temperature by the following relation;

$$\sigma_y = [A + B\varepsilon_p^n] \left[ 1 + C \ln \frac{\dot{\varepsilon}_p}{\dot{\varepsilon}_0} \right] \left[ 1 - \left( \frac{T - T_{room}}{T_{melt} - T_{room}} \right)^m \right] \quad (1)$$

where  $\varepsilon_p$  is equivalent plastic strain,  $\dot{\varepsilon}_p$  and  $\dot{\varepsilon}_0$  are the applied and reference deformation rate,  $T$ ,  $T_{room}$  and  $T_{melt}$  are applied, reference and melting temperature,  $A$  is the initial yield stress,  $B$  and  $n$  are constants describing hardening coefficient and exponent

**Table 2**

Johnson–Cook equation parameters for AISI 4340.

$A$ (MPa)	$B$ (MPa)	$n$	$C$	$m$	$\dot{\varepsilon}_0$ (1/s)	$T_{melt}$ (K)
792	510	0.26	0.014	1.03	1	1793

respectively,  $C$  and  $m$  are also constants describing the flow stress sensitivity to strain rate and temperature. Table 2 represents the Johnson–Cook parameters for AISI 4340 [29]. It should be noted that the dependency of flow stress on temperature has been neglected in the present simulation because shot peening is widely accepted to be a cold working process and any local heat rise at the surface would be quenched to the bulk quickly.

We also simulated 3D shot peening over a sequence of multiple impacts, as incorporation of a large number of impacts is crucial toward a realistic simulation of sever shot peening and the induced structural refinement. The basic principles of the 3D simulations (material behavior, initial and boundary condition and contact properties) are essentially similar to those of the 2D simulations. The main difference lies in the multiple impacts, which should represent a realistic and yet not too computationally demanding evolution of coverage. We employed a constrained random positioning method for each 100% increment of coverage, in which the center of every impact is forbidden to lie within  $0.4R$  of prior impact centers; where  $0.4$  is the ratio of a single impact indentation radius to the shot radius for parameters matching our experiment. It should be noted that this constraint does not mean there is no overlap, as any impact hitting  $0.4$ – $0.8R$  away from previous impact centers provides interaction of plastic zones. Furthermore, the history of random positioning is reset after each 100% increment of coverage leading to a realistic overlap simulation of multiple deformation events.

Based on some trial runs, the radius of the treated area for the 3D simulations of multiple impact was chosen to be 5 times the radius of the indentation induced by a single impact. To avoid edge effects, the target was considered to be a big enough cylindrical domain with the treated area at the middle. Full coverage (100%) at the treated area was attained with 42 impacts, and by extension 1300% coverage was achieved with 546 impacts. For a more detailed description, readers are referred to Ref. [30]. Fig. 1b shows the finite element model for multiple impacts. Since equivalent plastic strain is the output of the FE simulation and the input for the subsequent dislocation density model, our mesh convergence study was conducted on this parameter. The results converged for  $5 \mu\text{m}$  and  $20 \mu\text{m}$  element size in 2D and 3D models respectively.

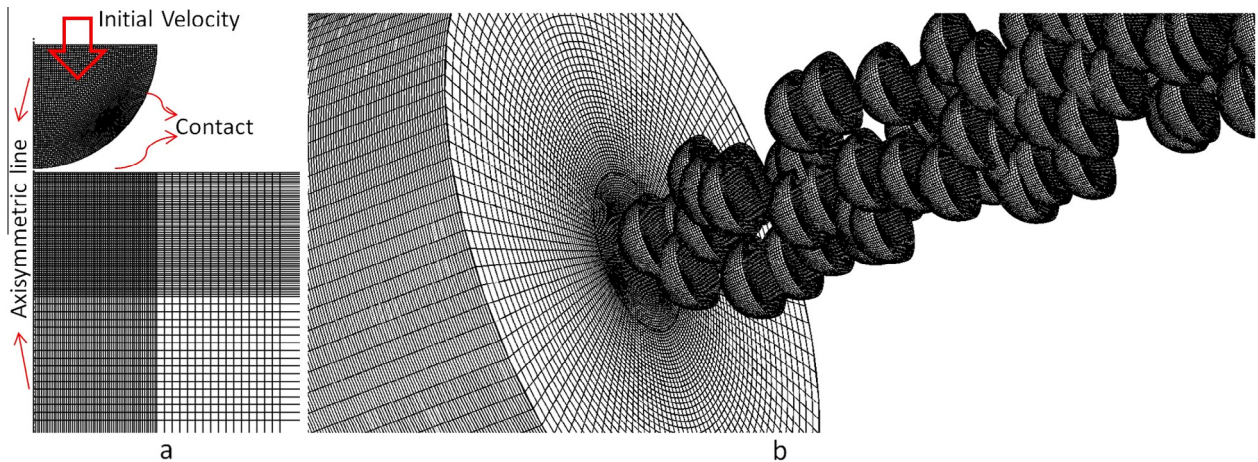


**Fig. 1.** Finite element model of (a) a single impact and (b) multiple impacts.

### 3.2. Dislocation density evolution model

Generation of a dislocation cell structure in the early stage of plastic deformation and its evolution to the final fine grain structure as deformation continues, is perhaps the most commonly accepted model of refinement due to large plastic strain. This occurs through continual decrease in the average grain size accompanied by accumulation of misorientation between neighboring dislocation cells [31]. Based on many earlier developments describing the stages of hardening in crystals deformed to various strain levels [32–37], Estrin et al. [38] proposed a 2D dislocation density model, sometimes called ETMB, consisting of two coupled differential equations for the evolution of cell and wall dislocation densities, such as is relevant to larger strains where a cell structure emerges. The model was generalized soon afterwards for 3D cases and arbitrary strain paths [39] and has become a useful framework to predict grain refinement in the last decade. This model is adopted in the present work to assess the grain refinement during severe shot peening. It should be underlined that the present model is intended to treat materials that deform by dislocation plasticity only and materials which undergo extensive deformation twinning are not treated by this model. The model begins with the reciprocal-parabolic relation between the average dislocation cell size and the total dislocation density:

$$d = \frac{K}{\sqrt{\rho_t}} \quad (2)$$

This relationship was presented in the early work of dislocation cell formation by Holt [40].  $K$  is taken to be an accumulated strain-dependent parameter [41,42] which quickly decreases from an initial to a saturated value with the accumulation of the total dislocation density:

$$K = K_\infty + (K_0 - K_\infty) \exp(-\beta \gamma^r) \quad (3)$$

where  $\gamma^r$  is the resolved shear strain. The total dislocation density can be expressed by a weighted sum of dislocation density in the cell walls (subscript “w”) and cell interior (subscript “c”).

$$\rho_t = f \rho_w + (1 - f) \rho_c \quad (4)$$

$$f = f_\infty + (f_0 - f_\infty) \exp(\gamma^r / \tilde{\gamma}) \quad (5)$$

Here,  $f$  represents the volume fraction of dislocation walls.  $f$  is assumed, as suggested by the phenomenological Eq. (5), to have a decreasing trend from an initial to a saturated value as plastic strain increases. The parameter  $\tilde{\gamma}$  is a constant that quantifies the rate of the descent.

The evolution of the dislocation population in the cell interior and cell walls is captured by a set of coupled differential equations, under a Taylor-type assumption that the shear strain is the same in both phases:

$$\frac{d\rho_c}{dt} = \alpha^* \frac{1}{\sqrt{3}} \frac{\sqrt{\rho_w} \dot{\gamma}^r}{b} - \beta^* \frac{6 \dot{\gamma}^r}{b d (1 - f)^{1/3}} - k_c \left( \frac{\dot{\gamma}^r}{\dot{\gamma}_0} \right)^{-1/n_c} \rho_c \quad (6)$$

$$\frac{d\rho_w}{dt} = \frac{6 \beta^* \dot{\gamma}^r (1 - f)^{2/3}}{b d f} + \frac{\sqrt{3} \beta^* \dot{\gamma}^r (1 - f) \sqrt{\rho_w}}{f b} - k_w \left( \frac{\dot{\gamma}^r}{\dot{\gamma}_0} \right)^{-1/n_w} \rho_w \quad (7)$$

The various terms in the right hand side of Eqs. (6) and (7) represent the contribution from different dislocation mechanisms. The first term in Eq. (6) represents the rate of dislocation generation in the cell interior due to activation of Frank-Read sources at the interface. The second term in Eq. (6) represents the fraction of dislocations that leave the cell interior towards the wall and become part of the wall structure. The last term in Eq. (6) accounts for the mutual annihilation of dislocations in the cell associated with cross slip of screw dislocations or climb of edge dislocations. The first

term in Eq. (7) represents the accommodation of the dislocations in the wall corresponding to the loss of cell interior dislocations. The second term describes dislocation generation in the walls due to activation of Frank-Read sources at the interface. Finally the last term in Eq. (7) accounts for annihilation of dislocations in the walls. Here  $b$  is the magnitude of the Burgers vector and coefficients  $\alpha^*$ ,  $\beta^*$ ,  $k_c$  and  $k_w$ , are numerical constants. The quantity  $\dot{\gamma}_0$  is a reference shear rate. The exponents  $n_c$  and  $n_w$  are constants here due to the assumption of an isothermal peening process.

In order to link the dislocation interactions to the mechanical behavior of material, one can express the flow stress of the material as the sum of two terms:

$$\sigma = \sigma_1 + \sigma_2 \quad (8)$$

In Eq. (8),  $\sigma_1$  represents a strain-independent contribution to the stress that originates from the resistance to dislocation glide (friction), not related to dislocation–dislocation interactions. This stress may be estimated from the yield stress of the un-deformed material [43]. In fact this term plays the same role as ‘A’ does in Eq. (1), and the self-consistency of Eq. (8) with Eq. (1) will be addressed in greater detail below where we introduce our method of optimizing the parameters in the dislocation density evolution model. The second term in Eq. (8) originates from dislocation–dislocation interactions and is strain and strain rate dependent. The resolved shear stress and the shear strain rate can be correlated to  $\sigma_2$  and equivalent strain rate via the Taylor factor:

$$\tau^r = \frac{\sigma_2}{M} \quad (9)$$

$$\dot{\gamma}^r = M \dot{\epsilon} \quad (10)$$

Resolved shear stress, describing the overall mechanical behavior of the cell-wall composite structure, can be correlated to the two developed resolved shear stresses in the cell and in the wall by a rule of mixtures:

$$\tau^r = f \tau_w^r + (1 - f) \tau_c^r \quad (11)$$

Relating these resolved shear stresses to their corresponding dislocation densities completes the set of equations:

$$\tau_w^r = \alpha G b \sqrt{\rho_w} \left( \frac{\dot{\gamma}^r}{\dot{\gamma}_0} \right)^{1/m^*} \quad (12)$$

$$\tau_c^r = \alpha G b \sqrt{\rho_c} \left( \frac{\dot{\gamma}^r}{\dot{\gamma}_0} \right)^{1/m^*} \quad (13)$$

where  $\alpha$  is a constant,  $G$  is shear modulus and  $m^*$  is the inverse strain rate sensitivity parameter.

Dislocation evolution has been linked to the variation of flow stress through the course of straining. It was shown that the model is able to successfully predict all stages of strain hardening at large strain [38,39], grain refinement under equal channel angular pressing [44,45], high pressure torsion [42] and Taylor impact test [43].

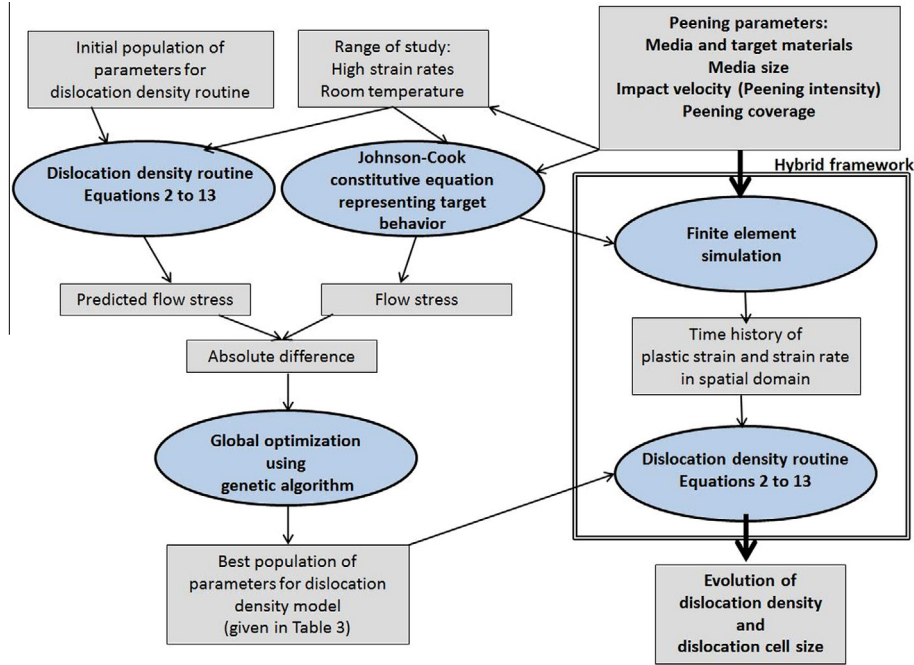
A routine was written in MATLAB [46] to represent the dislocation density evolution model described by Eqs. (2–13), and linked to the finite element simulation of peening described in Section 3.1. The time history of strain and strain rate at various depths in the target during peening was first calculated using finite element simulation on the basis of Eq. (1) for the material response. The resulting strains and strain rates experienced by the target were then evaluated using the dislocation density routine to estimate the dislocation structure evolution. Self-consistency of the mechanical model (Eq. (11)) and the microstructure-based model (Eq. (8)) was enforced by performing a global minimization using a genetic algorithm to find the best set of input parameters that minimizes the absolute difference



**Table 3**

Material parameters for AISI 4340 used in the dislocation density evolution model.

Tuned parameters							Other parameters												
$\alpha^*$	$\beta^*$	$k_i$	$k_w$	$n_i$	$n_w$	$m^*$	$b$ (m)	$M$	$\alpha$	$G$ (GPa)	$f_0$	$f_\infty$	$\dot{\gamma}_0$	$K_0$	$K_\infty$	$\bar{\gamma}$	$\beta$	$\rho_c^{t=0}$ (m <sup>-2</sup> )	$\rho_w^{t=0}$ (m <sup>-2</sup> )
0.154	0.078	18.6	32.8	89.8	90.3	60.8	$2.48 \times 10^{-10}$	3.06	0.25	82	0.25	0.06	$10^7$	100	1	3.2	0.26	$2.5 \times 10^{13}$	$5 \times 10^{13}$

**Fig. 2.** Schematic representation of the minimization procedures along with the hybrid framework.

between flow stress given by the Johnson–Cook constitutive equation (Eq. (1)) and predicted by the dislocation density routine for high strain rates ( $10^4$ ,  $10^5$ ,  $10^6$  s<sup>-1</sup>) at room temperature. Table 3 summarizes the seven tuned parameters for AISI4340 as well as other constants [38–45] used in the model. The schematic representation of the minimization procedures along with the hybrid framework is given in Fig. 2. The hybrid framework provides a direct connection between processing parameters such as media size, velocity and peening coverage to the resultant structure.

#### 4. Results

Fig. 3 shows the distribution of residual stress, equivalent plastic strain, total dislocation density and dislocation cell size after a single impact, the unit process of peening. Compressive residual stresses are developed in the subsurface layer after a single impingement (Fig. 3a), and the stored equivalent plastic strain correlates to microstructure evolution. Fig. 3b shows that the maximum plastic strain after a single impingement occurs in the immediate subsurface layer near the indentation edge where material piles up. As generation and rearrangement of dislocations accommodate the plastic deformation, it is not surprising that the maximum dislocation density (Fig. 3c) and the minimum cell size (Fig. 3d) are both located at the same point, where the plastic strain is maximum. As demonstrated in Fig. 3c, dislocation density increased by about two orders of magnitude after a single impact, for instance from  $3.1 \times 10^{13}$  to  $1.5 \times 10^{15}$  m<sup>-2</sup> at the most critical point. Based on the selected initial dislocation densities, the initial cell size was calculated to be approximately 18  $\mu$ m. As illustrated in Fig. 3d dislocation cell size was refined from 18 to 2.47  $\mu$ m.

This implies that significant structural refinement might occur even upon the first impact, but a single impact (and by extension coverage levels below about 100%) is not expected to produce a uniform layer of an ultrafine or nanocrystalline structure.

Fig. 4 summarizes the effect of processing parameters on the minimum cell size obtained by a single impact. As shot hardness increases, the cell size decreases initially but tends to saturate eventually. As shot radius increases, no considerable change in the level of refinement is expected. Shot velocity would appear to be the most influential processing parameter among the variables explicitly studied, as far as grain refinement and surface nanocrystallization is concerned in severe shot peening; as shot velocity increases higher refinement in cell size can be obtained and the trend is linearly ever-increasing over the range studied here.

Fig. 5 shows the surface and subsurface equivalent plastic strain distribution after conventional shot peening with 100% coverage and severe shot peening with 1000% coverage, using the parameters that match the experiments, namely shot velocity of 65 m/s, shot radius of 0.3 mm, and shot hardness of 48 HRC. The average surface plastic strain after conventional shot peening was around 0.5. The maximum plastic strain induced in the deformation localized area was around 1, while it significantly increased to 7.8 after severe peening with a more uniform distribution. One order of magnitude increase in the coverage (peening time) increased the induced plastic strain by one order of magnitude. The minimum amount of strain necessary for nanocrystallization was reported to be around 7–8 [15,16].

TEM observation of the top surface layer shown in Fig. 5c confirms nanocrystallization by severe shot peening. Nano-sized grains can be observed at the top surface. The simulation shows

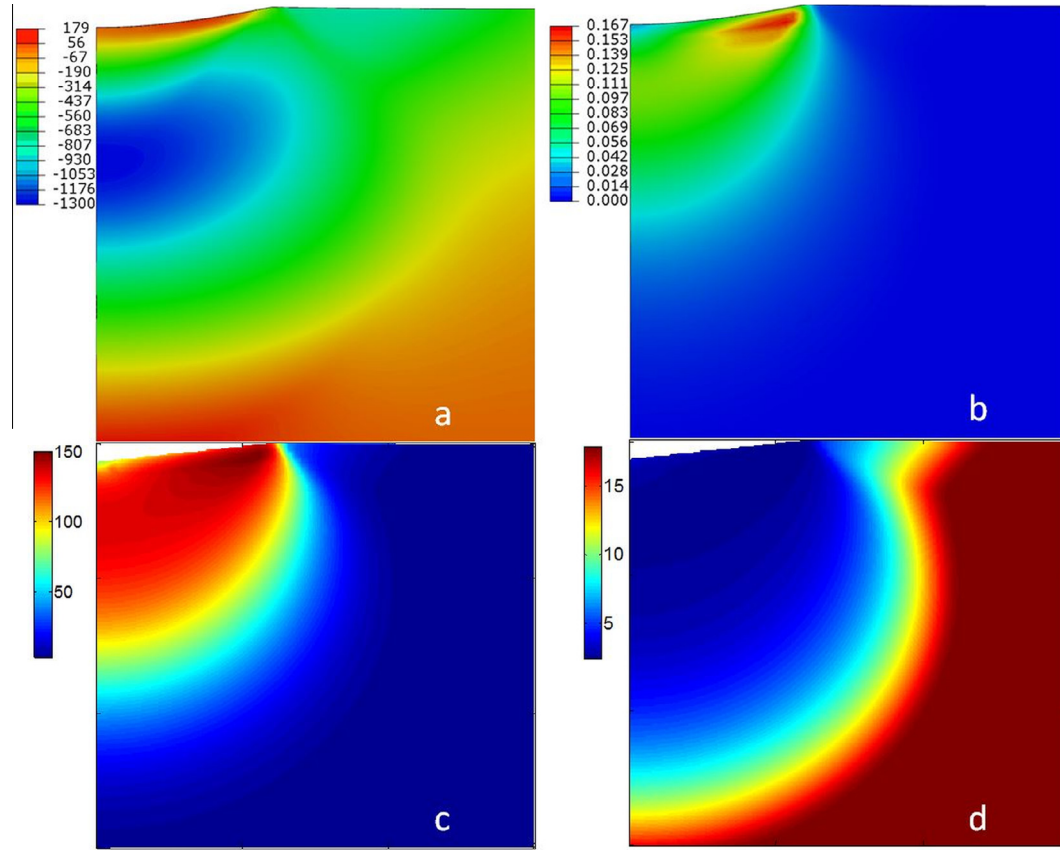


Fig. 3. Distribution of (a) residual stress (MPa), (b) equivalent plastic strain, (c) total dislocation density ( $10^{13} \text{ m}^{-2}$ ) and (d) dislocation cell size ( $\mu\text{m}$ ) after single impact.

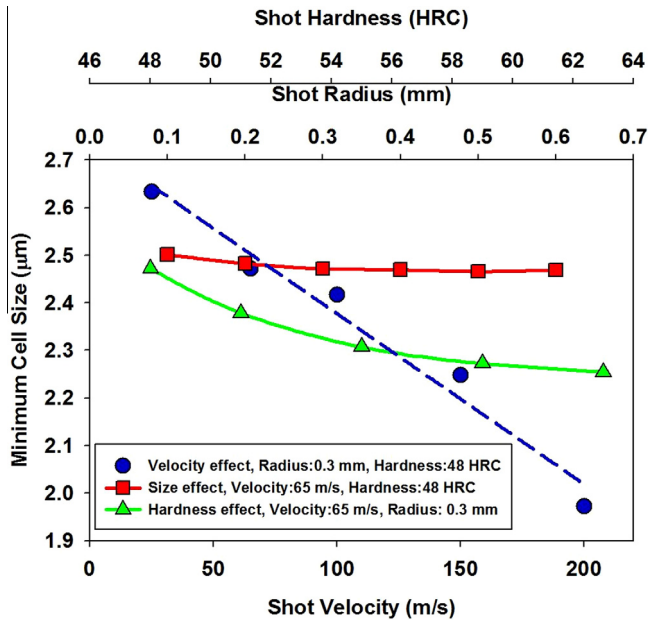


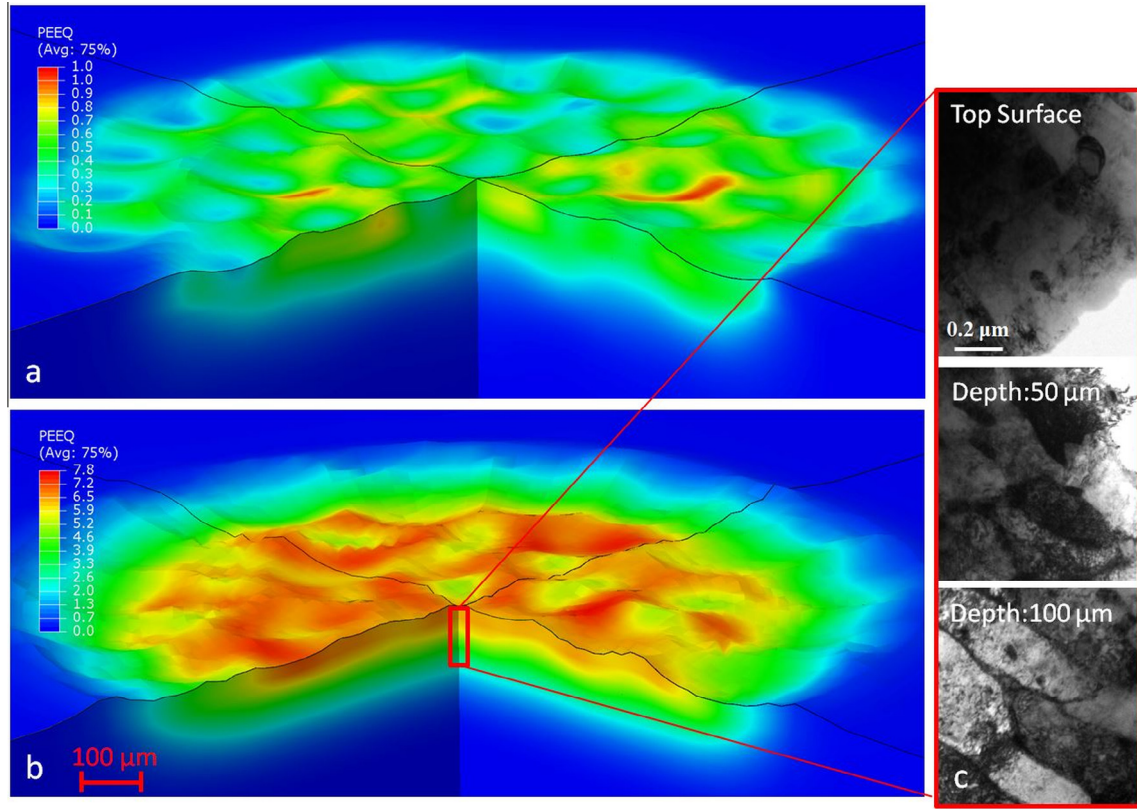
Fig. 4. Effect of processing parameters on the minimum cell size obtained after single impact, suggesting shot velocity to be the most influential processing parameter among the studied variables.

a relatively uniform distribution of plastic strain can be expected across the sample, with a significant gradient of plastic strain normal to the sample surface. This aligns with the gradient in the degree of structural refinement seen in the TEM micrographs.

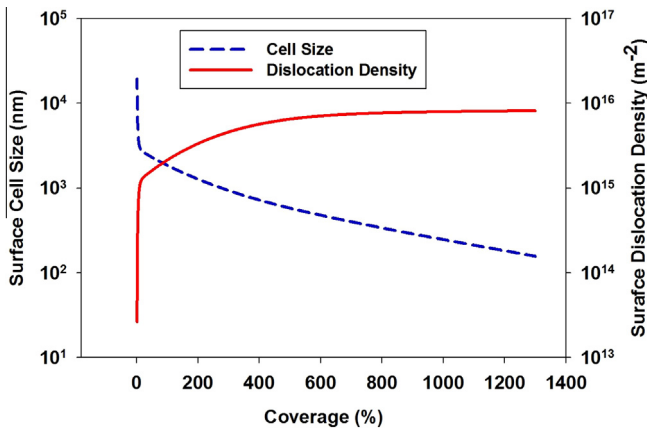
Fig. 6 shows the variation of surface dislocation density and cell size as coverage increases. Both parameters have been averaged over the treated surface. Surface dislocation density increases during the process as more shots hit the surface. A sharp increase can be seen in the early stage of deformation where dislocation density exceeds  $10^{15} \text{ m}^{-2}$ . Afterwards the rate of increase gradually decreases as dislocation density increases. The surface cell size accordingly follows the same trend, with many more impacts needed to refine the cell size as it approaches 100 nm. The trend affirms that subdivision of cells below a size of 100 nm is feasible at sufficiently high coverage by severe shot peening.

Fig. 7 shows the cross section SEM and TEM micrographs taken at various depths of the treated specimens. Nano-sized grains are observed at the top surface of severely deformed specimens (1000% and 1300% coverage). For 650% coverage the surface grains are in the ultra-fine regime. The average grain sizes measured by TEM at the surface are 370, 160 and 130 nm for 650%, 1000% and 1300% respectively. TEM micrographs clearly affirm that the higher the coverage is, the smaller the cell/grain size that results at the same depth for different specimens.

The shape of the grains at the very top surface is equiaxed. The same observation has also been reported for similar mechanical treatments [4–6,9,23,47]. As one moves away from the surface a duplex micro-structure appears. Equiaxed ultrafine cells and lamellar-shaped cells are observed. Lamellar-shaped cell structure with a width of 250–500 nm and a length of a few microns can be seen in Fig. 7 for the coverage level of 650% at the depth of 200  $\mu\text{m}$ . Inside these lamellar structures, at some points, smaller equiaxed cells can also be observed. SEM images of 100% and 200% coverage levels (conventionally peened specimens) show the initial microstructure is sheaf-shaped bainite. As one moves from



**Fig. 5.** Surface and in-depth distribution of equivalent plastic strain after (a) shot peening with 100% coverage and (b) severe shot peening with 1000% coverage. (c) TEM observation of the surface layers after severe peening.



**Fig. 6.** Variation of surface cell size and dislocation density with coverage.

300 μm depth towards the surface, SEM micrographs demonstrate the initial sheaf-shaped needles or plates are subdivided to finer needles and plates, possibly as a result of multiple impingements and superimposed overlapping strain fields. These observations suggest that the plastic strain is accommodated by generation, accumulation and re-arrangement of dislocations in the form of lamella-shape cells at first, followed by cutting of the original lamellae. As plastic strain increases and in order to minimize the total energy of the system, lamella walls and consecutively intersecting dislocation arrays transform into sub-boundaries. Further increasing plastic strain is accompanied by accumulation of misorientation between neighboring dislocation cells and gradually transforms them to the final fine grain structure. This microstructural refinement is also reflected in the selective area

electron diffraction (SAED) patterns shown in Fig. 7, where the streak spots demonstrate that the elongated lamellae are subdivided by dislocations. This is a local microstructural difference observed on the top surface after severe peening. This refined structure is retained up to a depth of 100 μm in both 1000 and 1300% coverage conditions (see the SAED patterns at 100 μm depth), but not in the peened sample with 650% coverage.

## 5. Discussion

Fig. 8 shows the depth distribution of cell size resulting from the numerical modeling as well as the ones experimentally measured by SEM and TEM. The agreement between the simulations and the experiments is good, with no fitting parameters in the present use of the model. The maximum refinement occurs at the surface, and no large variation of cell size (note the log scale) is observed in the top surface layer to a depth of about 50 μm. This region in fact corresponds to the equiaxed nano-sized or ultrafine grains structure in severely peened specimens. The variation then is followed by a gradual increase of cell size up to around 200 μm where it encounters a sharp rise towards the grain size of the initial structure. A duplex structure containing both equiaxed and lamellar-shaped cells appears at this region. A similar trend has been experimentally observed elsewhere [5] where a slight increase of cell size from surface to a certain depth is followed by a rapid rise to the micrometer regime in high energy peened carbon steel. Superimposed data from TEM and SEM measurements affirms that the numerical framework is able to correctly simulate the gradient. TEM measurements tend to underestimate the cell size in deeper regions where the structure is mainly micron-sized lamellar cells, whereas chemical etching improves



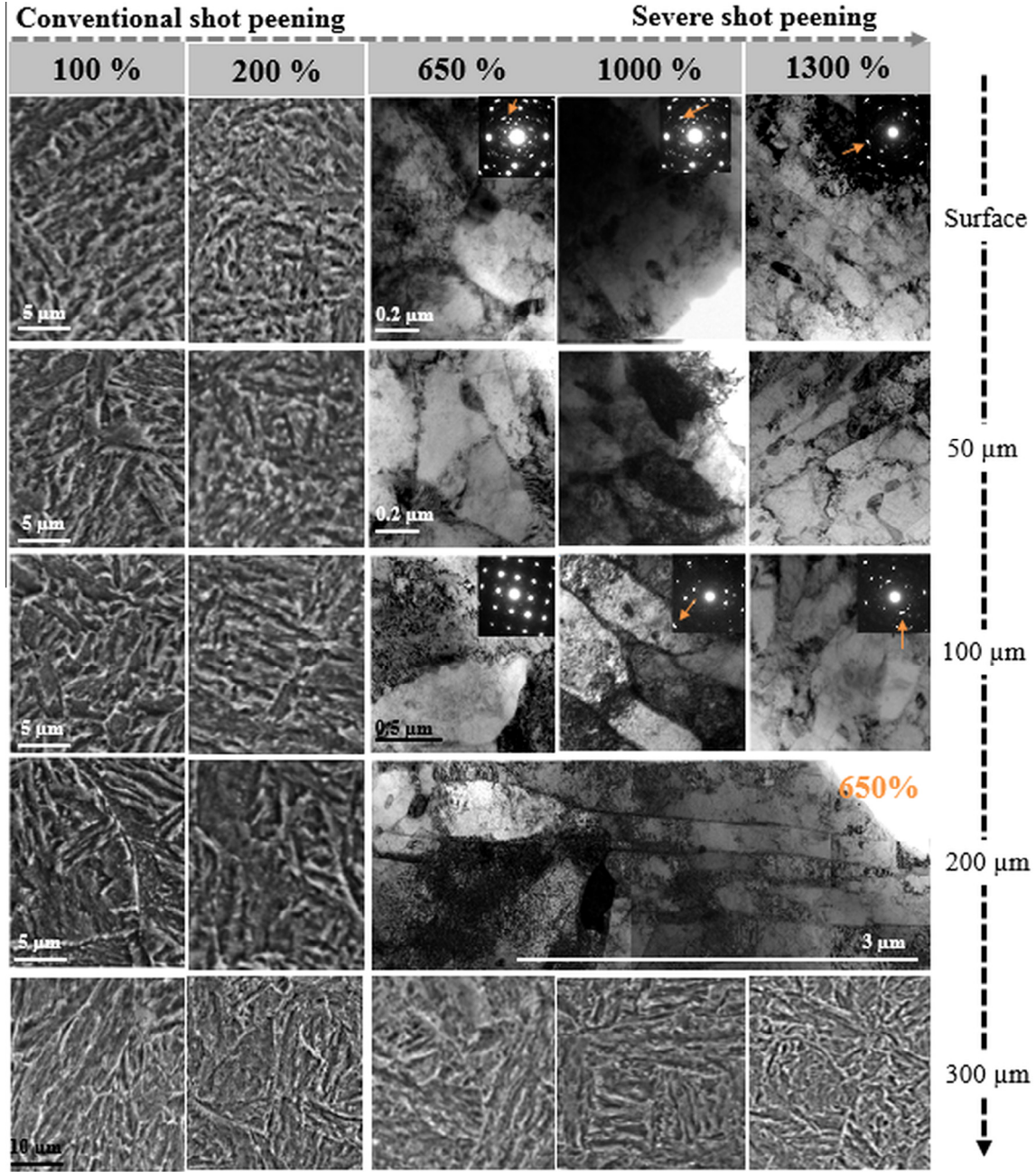


Fig. 7. Cross section SEM and TEM micrographs taken at various depths of the treated specimens.

contrast and may account for the apparently more accurate cell size measurements made by SEM for the coarser structures.

The numerical framework developed in this study is able not only to predict the refinement after severe peening, but also to support some related experimental observations of which five are discussed. First, Umemoto et al. [15] experimentally observed that a nanocrystalline layer is formed along the edge of the crater after 8 particle impacts at the same point. This can be explained by the present simulation (Fig. 3b–d) that shows a comparable point of critical refinement after a single impact. Second, smaller media fired at higher velocity appeared to be more effective than larger media fired at lower velocity in forming a NC surface layer; even though the latter case conveyed higher kinetic energy with respect to the former case [17,18]. This could be attributed to the fact that shot velocity, as shown in Fig. 4, is more influential than media size for grain refinement. Third, the trend of dislocation density

evolution shown in Fig. 6 is compatible with the argument on the limit of dislocation density and refinement in severely deformed iron which estimated the limit of dislocation density to be on the order of  $10^{16} \text{ m}^{-2}$  [48].

Fourth, experimental measurements of the yield stress of surface nano-crystallized low carbon steel by high energy shot peening, showed a pronounced increase of yield strength after 30 min peening while the strength saturated upon further increasing the treatment time to 60, 90 and 180 min [5]. As coverage and dislocation density are directly related to peening time and strength respectively, the trend of dislocation density variation with coverage, given in Fig. 6, are in qualitative agreement with the reported experiments. Finally, an important outcome of the numerical result depicted in Fig. 8 is that as coverage increases, the cell size in the surface and subsurface layers decreases and the thickness of the nano-crystallized or refined layer increases. However, the trend



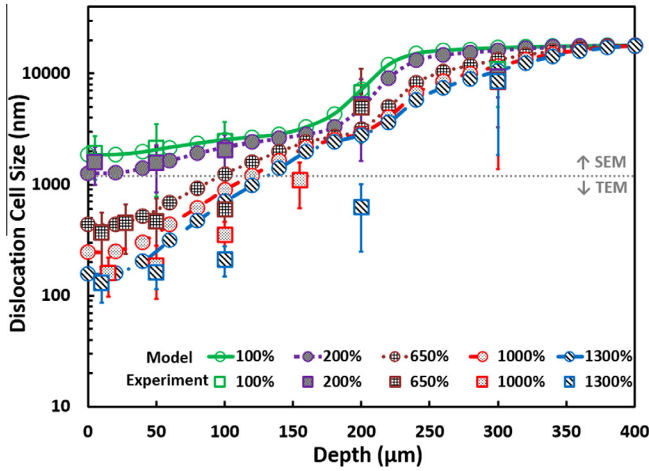


**Fig. 8.** In-depth variation of dislocation cell size; comparison of numerical simulation and experimental measurements.

suggests that the thickness of the refined layer saturates at very high coverage. This finding is also supported by experiments. It was shown that the thickness of the NC layer formed by high coverage shot peening initially increases with peening time [15], but eventually remains unchanged after a certain level of coverage [47,49]. However, measurement of the grain size at a depth of 10  $\mu\text{m}$  revealed no such saturation with coverage [47].

It is important to note that other microstructural evolution besides dislocation density and grain size changes are also possible. Although we have not extensively studied it in the present

system, peening clearly can cause phase evolution as well. TEM images taken from the top surface and at 200  $\mu\text{m}$  depth of the peened specimen with 1300% coverage are shown in Fig. 9. Two interesting features can be observed on the top surface shown in Fig. 9a. The first is dissolution of cementite. This can be realized by the trace comprising small particles ( $<100\text{ nm}$ ) of spherical shape, which are generally arrayed (but not necessarily oriented) along a  $\langle 110 \rangle$  direction. Completely different features, on the other hand, are observed at 200  $\mu\text{m}$  in depth (Fig. 9b), where cementite domains of approximately 200 nm lie within and in between ferrite plates. This suggests microstructural refinement by severe shot peening is also accompanied by dissolution of cementite. Dissolution of cementite in the ferritic matrix has also been reported in high coverage peened Fe-0.80C with an initial spheroidite structure [15,16].

Another observation is that a considerable number of nano-sized particles are precipitated at the top surface region as shown in Fig. 10, and appear to likely be  $\text{M}_2\text{C}$ -type carbides. These particles were characterized using their intrinsic orientation relationship with the matrix; needle or rod-shaped  $\text{M}_2\text{C}$  carbide generally has an orientation relationship with the martensite matrix;  $(110)_a // (0001)_{\text{M}_2\text{C}}$ ,  $[100]_a // [2110]_{\text{M}_2\text{C}}$ . In other words, the  $\text{M}_2\text{C}$  carbide precipitation can be found in  $\langle 100 \rangle$  cube directions of the  $[100]$  zone-axis. This result is also confirmed by the SAED patterns shown in Fig. 7. The diffraction spots at a smaller distance from the direct beam at the surface are larger than those at 200  $\mu\text{m}$  depth. This indicates the existence of other phases, especially carbides, different from the bcc matrix. These microstructural findings suggest that severe plastic deformation by shot peening can lead not only to microstructural refinement by introduction of a large density of dislocations but also to the

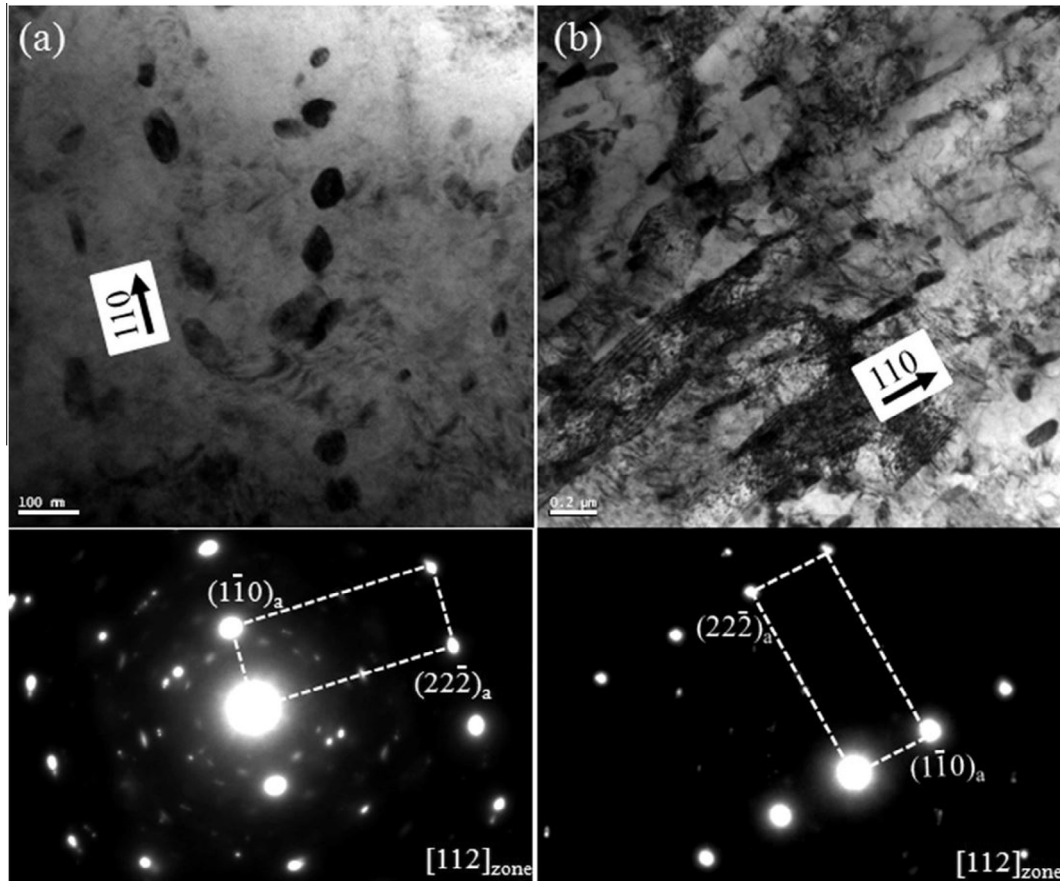


**Fig. 9.** TEM images taken from (a) top surface and (b) 200  $\mu\text{m}$  depth of peened specimen with 1300% coverage.

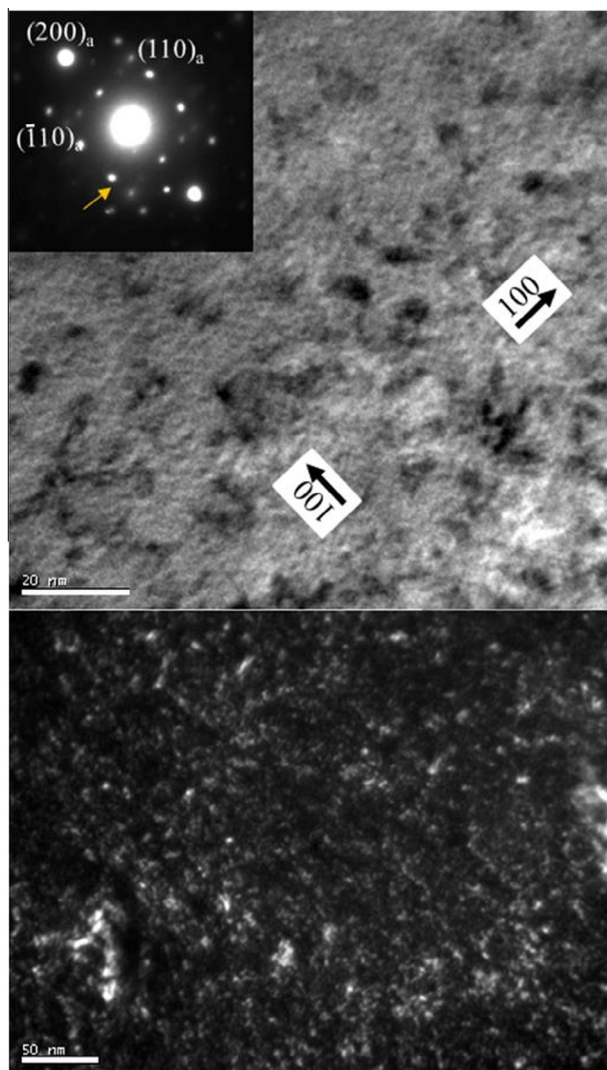


**Fig. 10.** Bright and dark field TEM image taken from the top surface of peened specimen with 1300%; nano-sized carbide precipitation at two different magnifications.

dissolution of cementite and subsequent nano-sized carbide precipitation.

## 6. Conclusion

Surface nanocrystallization by severe shot peening was assessed by SEM and TEM observations, and a hybrid numerical framework was developed to simulate the structural refinement. The model relates the process parameters to structural evolution, and to the resulting mechanical properties of the structure. On the basis of the results the following conclusions can be drawn:

- Air blast shot peening is able to generate a nanostructured surface layer on high strength low alloy steel using conventional media, a typical peening impact velocity and a high level of coverage. This is technologically promising as air blast shot peening has a lower cost and more flexibility as compared to other kinds of severe peening, and can be applied on a variety of components.
- The average grain sizes measured by TEM at the surface of severely peened specimens are 370, 160 and 130 nm for 650%, 1000% and 1300% coverage respectively. The degree of

refinement increases as the coverage increases, mainly due to generation, accumulation and re-arrangement of dislocations in the form of lamella-shape cells at first, followed by cutting of the original lamellae by intersecting dislocation arrays for the examined high strength low alloy steel.

- The hybrid simulation framework consisting of finite element simulation and a dislocation density evolution model produced satisfactory agreement with the experimentally measured grain/cell size.
- The model also reveals that the maximum refinement after a single impingement occurs in the immediate subsurface layer at the edge of the crater, and that increasing media velocity is more effective than increasing its size or hardness in producing grain refinement.
- The plastic strain distribution after conventional peening showed an average surface value around 0.5 with a maximum value around 1 in the deformation localized area. The corresponding surface cell/grain size was around 2  $\mu\text{m}$ . One order of magnitude increase in the coverage (peening time) increased the induced plastic strain by one order of magnitude. Finite element simulation shows that at such coverage levels, a relatively uniform distribution of plastic strain can be expected across the peened sample, with a significant gradient of plastic strain normal to the sample surface. One order of magnitude increase in the coverage, from the conventional level to severe, also decreased the surface cell/grain size by one order of magnitude.
- The TEM observations show that other microstructural evolution besides dislocation density and grain size changes are also possible by severe shot peening; the dissolution of cementite and subsequent nano-sized carbide precipitation were observed in the present case.

The success of the present model in matching the properties and structure evolution of the experimental material provides a direct connection between the processing parameters and the resulting surface nanostructure. It is hoped that such a tool could be useful in the practical design of a shot peening operation aimed at a target surface nanostructure.

## Acknowledgements

HJLV and CAS acknowledge the support of the US Army Research Office at MIT, through the Institute for Soldier Nanotechnologies. SMHG and MG acknowledge the support of the Scuola Interpolitecnica di Dottorato for the program of “Nanotechnologies and Nanostructured Innovative Materials”, the Politecnico di Milano International Fellowship, and thank Dr. Atieh Moridi from MIT for valuable discussions. KSC acknowledges the support of Basic Science Research Program (2009-0093814) through the National Research Foundation of Korea (NRF) funded by the Ministry of Education.

## References

- [1] K.S. Kumar, H. Van Swygenhoven, S. Suresh, *Acta Mater.* 51 (2003) 5743.
- [2] M.A. Meyers, A. Mishra, D.J. Benson, *Prog. Mater. Sci.* 51 (2006) 427.
- [3] K. Lu, J. Lu, *J. Mater. Sci. Technol.* 15 (1999) 193.
- [4] N.R. Tao, M.L. Sui, J. Lu, K. Lu, *Nanostruct. Mater.* 11 (1999) 433.
- [5] G. Liu, S.C. Wang, X.F. Lou, J. Lu, K. Lu, *Scr. Mater.* 44 (2001) 1791.
- [6] N. Tao, H. Zhang, J. Lu, K. Lu, *Mater. Trans.* 44 (2003) 1919.
- [7] Z.B. Wang, N.R. Tao, S. Li, W. Wang, G. Liu, J. Lu, K. Lu, *Mater. Sci. Eng. A* 352 (2003) 144.
- [8] D. Li, H.N. Chen, H. Xu, *Appl. Surf. Sci.* 255 (2009) 3811.
- [9] G. Liu, J. Lu, K. Lu, *Mater. Sci. Eng. A* 286 (2000) 91.
- [10] H.W. Zhang, Z.K. Hei, G. Liu, J. Lu, K. Lu, *Acta Mater.* 51 (2003) 1871.
- [11] Y. Lin, J. Lu, L. Wang, T. Xu, Q. Xue, *Acta Mater.* 54 (2006) 5599.
- [12] K. Wang, N.R. Tao, G. Liu, J. Lu, K. Lu, *Acta Mater.* 54 (2006) 5281.
- [13] X. Wu, N. Tao, Y. Hong, B. Xu, J. Lu, K. Lu, *Acta Mater.* 50 (2002) 2075.

- [14] Guagliano M. Severe Shot Peening to Obtain Nanostructured Surfaces: Processes, Properties and Application., in: Baiker S (Ed.). 4th ed. Wetzikon: Metal Finishing News; 2014.
- [15] M. Umemoto, Y. Todaka, K. Tsuchiya, *Mater. Trans.* 44 (2003) 1488.
- [16] M. Umemoto, *Mater. Trans.* 44 (2003) 1900.
- [17] Y. Todaka, M. Umemoto, K. Tsuchiya, *Mater. Trans.* 45 (2004) 376.
- [18] J.L. Liu, M. Umemoto, Y. Todaka, K. Tsuchiya, *J. Mater. Sci.* 42 (2007) 7716.
- [19] S.M. Hassani-Gangaraj, A. Moridi, M. Guagliano, A. Ghidini, M. Boniardi, *Int. J. Fatigue* 62 (2014) 67.
- [20] S.M. Hassani-Gangaraj, A. Moridi, M. Guagliano, A. Ghidini, *Mater. Des.* 55 (2014) 492.
- [21] S.M. Hassani-Gangaraj, A. Moridi, M. Guagliano, *IOP Conf. Ser. Mater. Sci. Eng.* 63 (2014) 012038.
- [22] K. Lu, J. Lu, *Mater. Sci. Eng. A* 375–377 (2004) 38.
- [23] N.R. Tao, Z.B. Wang, W.P. Tong, M.L. Sui, J. Lu, K. Lu, *Acta Mater.* 50 (2002) 4603.
- [24] S. Bagherifard, R. Ghelichi, M. Guagliano, *Surf. Coat. Technol.* 204 (2010) 4081.
- [25] M. Guagliano, *J. Mater. Process. Technol.* 110 (2001) 277.
- [26] W.H. Walton, *Nature* 162 (1948) 329.
- [27] Dassault Systemes, ABAQUS 6.10-1 User's Manual, 2010.
- [28] S.A. Meguid, G. Shagal, J.C. Stranart, *Int. J. Impact Eng.* 27 (2002) 119.
- [29] G.R. Johnson, W.H. Cook, *Eng. Fract. Mech.* 21 (1985) 31.
- [30] S.M.H. Gangaraj, M. Guagliano, G.H. Farrahi, *Surf. Coat. Technol.* 243 (2014) 39.
- [31] Y. Estrin, A. Vinogradov, *Acta Mater.* 61 (2013) 782.
- [32] U.F. Kocks, *J. Eng. Mater. Technol. Trans. ASME* 98 (Ser. H) (1976) 76.
- [33] H. Mecking, U.F. Kocks, *Acta Metall.* 29 (1981) 1865.
- [34] M. Zehetbauer, V. Seumer, *Acta Metall. Mater.* 41 (1993) 577.
- [35] H. Mughrabi, *Acta Metall.* 31 (1983) 1367.
- [36] F.B. Prinz, A.S. Argon, *Acta Metall.* 32 (1984) 1021.
- [37] W.D. Nix, J.C. Gibeling, D.A. Hughes, *Metall. Trans. A* 16 (1985) 2215.
- [38] Y. Estrin, L.S. Tóth, A. Molinari, Y. Bréchet, *Acta Mater.* 46 (1998) 5509.
- [39] L.S. Tóth, A. Molinari, Y. Estrin, *J. Eng. Mater. Technol. Trans. ASME* 124 (2002) 71.
- [40] D.L. Holt, *J. Appl. Phys.* 41 (1970) 3197.
- [41] R. Lapovok, F.H. Dalla Torre, J. Sandlin, C.H.J. Davies, E.V. Pereloma, P.F. Thomson, Y. Estrin, *J. Mech. Phys. Solids* 53 (2005) 729.
- [42] Y. Estrin, A. Molotnikov, C.H.J. Davies, R. Lapovok, *J. Mech. Phys. Solids* 56 (2008) 1186.
- [43] V. Lemiale, Y. Estrin, H.S. Kim, R. O'Donnell, *Comput. Mater. Sci.* 48 (2010) 124.
- [44] S.C. Baik, Y. Estrin, H.S. Kim, R.J. Hellmig, *Mater. Sci. Eng. A* 351 (2003) 86.
- [45] P.W.J. McKenzie, R. Lapovok, Y. Estrin, *Acta Mater.* 55 (2007) 2985.
- [46] MATLAB 7.10.0 Release 2010, The MathWork, Inc., United States, n.d.
- [47] Y. Todaka, M. Umemoto, Y. Watanabe, A. Yamazaki, C. Wang, K. Tsuchiya, *ISIJ Int.* 47 (2007) 157.
- [48] S. Takaki, *Mater. Sci. Forum* 426–432 (2003) 215.
- [49] J.G. Li, M. Umemoto, Y. Todaka, K. Tsuchiya, *J. Alloys Compd.* 434–435 (2007) 290.